Chapter 13
Applications of Sensing for Disease Detection

Ana Isabel de Castro Megías, Claudia Pérez-Roncal, J. Alex Thomasson, Reza Ehsani, Ainara López-Maestresalas, Chenghai Yang, Carmen Jarén, Tianyi Wang, Curtis Cribben, Diana Marin, Thomas Isakeit, Jorge Urrestarazu, Carlos Lopez-Molina, Xiwei Wang, Robert L. Nichols, Gonzaga Santesteban, Silvia Arazuri, and José Manuel Peña

Abstract The potential loss of world crop production from the effect of pests, including weeds, animal pests, pathogens and viruses has been quantified as around 40%. In addition to the economic threat, plant diseases could have disastrous consequences for the environment. Accurate and timely disease detection requires the use of rapid and reliable techniques capable of identifying infected plants and providing the tools required to implement precision agriculture strategies. The combination of suitable remote sensing (RS) data and advanced analysis algorithms makes it possible to develop prescription maps for precision disease control. This chapter shows some case studies on the use of remote sensing technology in some one of the world's major crops; namely cotton, avocado and grapevines. In these case studies, RS has been applied to detect disease caused by fungi using different acquisition platforms at different scales, such as leaf-level hyperspectral data and

A. I. de Castro Megías (✉)
National Institute for Agricultural and Food Research and Technology (INIA), Madrid, Spain AU1

Institute for Sustainable Agriculture (IAS-CSIC), Cordoba, Spain
e-mail: anadecastro@ias.csic.es

C. Pérez-Roncal · C. Jarén · D. Marin · J. Urrestarazu · C. Lopez-Molina · G. Santesteban · S. Arazuri
School of Agricultural Engineering and Biosciences, Public University of Navarre (UPNA), Pamplona, Spain

J. A. Thomasson
Mississippi State University, Mississippi State, MS, USA
e-mail: thomasson@tamu.edu

R. Ehsani
University of California, Merced, CA, USA

A. López-Maestresalas · C. Yang
USDA Agricultural Research Service, College Station, TX, USA

R. Kerry, A. Escolà (eds.), *Sensing Approaches for Precision Agriculture*, Progress in Precision Agriculture,
https://doi.org/10.1007/978-3-030-78431-7_13

canopy-level remote imagery taken from satellites, manned airplanes or helicopter, and UAVs. The results proved that remote sensing is useful, efficient and effective for identifying cotton root rot zones in cotton fields, laurel wilt-infested avocado trees and esca-affected vines, which would allow farmers to optimise inputs and field operations, resulting in reduced yield losses and increased profits.

Keywords Crop disease · Leaf and canopy level · Image analysis · Spectral analysis · UAVs · Multispectral and hyperspectral imaging · Prescription map AU2

13.1 Introduction

AU3

The potential yield of agricultural crops can be affected by biotic and abiotic stress factors that can reduce the quality and quantity of production. It has been estimated that around 40% of world crop production is lost due to the impact of pests, including weeds, animal pests, pathogens and viruses (Oerke and Dehne 2004). Moreover, in terms of the efficacy of actual crop protection practices, the control of diseases caused by fungi and bacteria is considerably less than protection obtained for other pests (Oerke and Dehne 2004). In addition, plant diseases are not only an economic threat, but could also have disastrous consequences for the environment, as new diseases and the re-emergence of controlled ones are developing at an alarming rate in crops around the world with transfers between hosts, global climate change and the use of some intensive management practices to increase productivity (Howden et al. 2007). Precision disease control is therefore a challenging goal in agriculture that could assist growers in decision-making to improve crop yields and reduce economic costs and environmental risks.

Traditionally, diagnostic methods consist of visual inspection of suspicious trees, collecting symptomatic plants and laboratory analyses, including microscopic evaluation, and molecular, serological and microbiological diagnostic techniques. These methods are costly and time-consuming, especially when disease symptoms are similar to those caused by abiotic stress such as nutrient and water deficiency,

T. Wang
Texas A&M AgriLife Research, Dallas, TX, USA

C. Cribben
Growers, LLC, Garner, NC, USA

T. Isakeit
Texas A&M University, College Station, TX, USA

X. Wang
Nanjing Forestry University, Xuanwu, China

R. L. Nichols
Cotton Incorporated, Cary, NC, USA

J. M. Peña
Institute of Agricultural Sciences (ICA-CSIC), Madrid, Spain

making visual diagnosis of the disease very complicated. In addition, visual estimation is subject to the individual's experience and, therefore, to human bias (Mahlein 2016). Accurate and timely disease detection requires the use of rapid and reliable techniques to collect and process data, based on spatial and temporal information on the crop in the field. In that sense, techniques capable of detecting infected plants before they show symptoms noticeable to the human eye would allow better crop management and mitigate the spread of disease (De Castro et al. 2015a).

The need for robust and timely indicators of disease is increasing the focus of the agricultural sector to find technological advances for monitoring plant health. The main objective of such advances is to provide growers with tools to implement precision agriculture (PA) methods that reduce the economic and environmental costs related to agricultural activity and adapt to the social demands for improved food security and the sustainability of agricultural production systems. In this context, remote sensing (RS) systems play a key role through the application of powerful technologies, such as new terrestrial (tractor, carriers, robots) or remote platforms (satellite, manned aircraft and unmanned aerial vehicles -UAVs), and multispectral, hyperspectral and thermal sensors, which have immense potential for monitoring the health status of crops (Zhang et al. 2019). Sensors can provide dense information for the whole field with less expense and can also provide information at wavelengths not visible to the human eye making earlier disease detection possible. In addition, the development of increasingly powerful algorithms for image and data analysis (e.g. multivariate analysis, machine learning and deep learning) enables the discovery of hidden patterns and unknown correlations between the factors involved in the disease development. However, the data analysis necessary can be time-consuming and requires automation once sound approaches have been developed. The combination of suitable remote sensing data and advanced analysis algorithms makes it possible to develop prescription maps for site-specific pest management programs in sustainable crop production.

In this chapter, case studies on the use of remote sensing techniques in arable crops, horticulture and viticulture, accounting for some of the world's major crops; namely cotton, avocado and grapevines, are described. In all the cases, RS has been applied to detect disease caused by fungi using data from several types of RS platform. Images from satellite, manned plane and UAVs were used to map cotton root rot (CRR) for site-specific application of fungicide using tractor pulled variable-rate (VR) control systems. In the case of avocado, the study describes the spatial and spectral properties for the diagnosis of laurel wilt (Lw) using spectral information and remote images from helicopter flights at low altitude. In addition, another widespread avocado disease, i.e. Phytophthora root rot, and abiotic factors causing similar symptoms were evaluated. In the grapevine case study, a hyperspectral (HS) imaging system was employed on *esca* diseased leaves to distinguish between visually asymptomatic and symptomatic leaves at the laboratory scale using multivariate data analysis and several pre-processing imaging techniques.

13.2 Case Study 13.1. Detecting Cotton Root Rot disease for Precision Fungicide Application

13.2.1 Introduction

Cotton Root Rot (CRR), caused by the soilborne fungus *Phymatotrichopsis omnivora*, has been a major disease in cotton crops in the southwestern USA (mainly Texas and Arizona) since first described by Pammel (1888). From 2002 to 2011, roughly 6% of the Texas cotton crop was lost to CRR annually (NCC 2013). Roots of infected plants rot, and then the plants wilt and die quickly with the leaves still attached. Symptoms in a cotton crop begin during vegetative growth but typically are more noticeable during flowering and fruit development. The CRR tends not to affect entire fields; instead it begins at various points in a field and typically spreads from these foci throughout the growing season (Smith et al. 1962) in irregular, mainly circular patterns (Lyda 1978). Diseased areas (Fig. 13.1a) range in size from less than a square metre to several hectares and expand as the season progresses, especially in rainy years. Moreover, CRR tends to occur from year to year in virtually the same areas within fields (Yang et al. 2016). Therefore, remote sensing (RS) imagery recorded late in one growing season and used to detect CRR zones can be useful to predict their occurrence in future seasons.

Over many decades, several treatments have been evaluated for disease control with little or no success. But in 2008 Topguard fungicide (FMC Corp., Philadelphia, PA, USA), containing the active ingredient flutriafol, was found in a research trial to be effective at controlling CRR (Isakeit et al. 2009) and has been available to growers since 2012. Growers who applied the fungicide on their fields achieved lower CRR incidence, larger yields, and better fibre quality on affected fields (Drake et al. 2013; Yang et al. 2014). The most effective method of fungicide application is during planting, which is many weeks before the appearance of symptoms in plants growing in an infested field.

13.2.2 Methods

Now that a successful treatment for CRR has been found, fields with a history of CRR are commonly treated uniformly, even though the fungicide is expensive (up to $125 USD per ha in 2019) and the grower is aware that only a portion of the field is infected. Uniform treatment ensures that all existing and potential new infected areas are treated because it is not known whether infected areas will expand from year to year. Furthermore, growers historically have not had ready access to site-specific application equipment and prescription maps that could potentially be developed from RS imagery. The following descriptions illustrate the use of three types of RS data in field studies to map areas of diseased cotton for site-specifically applying fungicide, as well as describing the advantages and disadvantages of each method, and potential future advances in the technology.

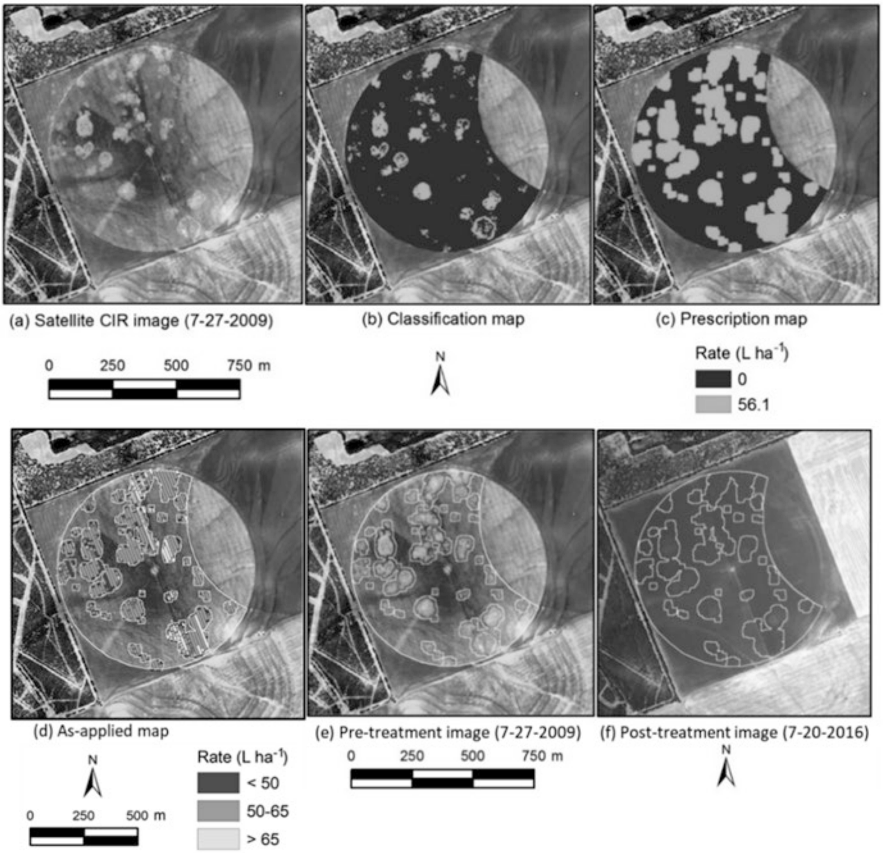

Fig. 13.1 (**a**) A 2009 GeoEye-1 satellite colour-infrared (CIR) image of a 41-ha cotton field in southern Texas with areas of CRR, (**b**) a two-zone classification map of the field, in which light-grey spots are classified as infected and the dark-grey area is classified as healthy, (**c**) a prescription map of the field in which only the light-grey spots were treated with fungicide, (**d**) the as-applied map for actual fungicide applied during planting, (**e**) the original satellite image of the field with fungicide-application zones delineated, and (**f**) the post-treatment image, showing that virtually no disease is evident in the field in 2016 after the precision fungicide application. (Adapted from Yang et al. 2018. Used with permission)

13.2.2.1 Satellite Remote Sensing

Until recently, available satellite data (e.g. Landsat) did not have adequate spatial resolution to map CRR precisely in a field. Newer satellite systems, however, are reaching a level of resolution (1.0 to 2.0 m per pixel) that can be useful in mapping CRR. Yang et al. (2018) used a GeoEye (DigitalGlobe, Inc., Longmont, CO, USA) satellite scene acquired on July 27, 2009, to detect CRR in a southern Texas field with a history of CRR (Fig. 13.1a). Image-acquisition timing was late in the growing season when the full extent of CRR was expressed, but prior to pre-harvest defoliation so that green leaves remained on the live plants. The scene included four image bands (red, green, blue and near-infrared; or RGB plus NIR) at fairly high resolution (2 m).

A prescription map based on the satellite image was created in eight steps. (1) A field boundary was defined for the field to create an area of interest (AOI). (2) A normalised difference vegetation index (NDVI) image was created for the AOI. Pixels with smaller NDVI values were generally associated with CRR-infected zones, while those with larger values were associated with non-infected zones. (3) The NDVI images were classified with Imagine software (Erdas Inc., Norcross, GA, USA) into CRR-infected and non-infected zones by ISODATA (iterative self-organizing data analysis) unsupervised classification (Campbell 2002). The ISODATA method was initiated with two classes having arbitrary class means based on the NDVI image statistics. Each pixel was assigned to the class closest to the NDVI mean. Once all image pixels were assigned to a class, the NDVI means of the two classes were recalculated and used for subsequent iteration. The process was repeated until the number of iterations reached a prescribed limit or the percentage of changed pixels was within a small prescribed tolerance of 0% between iterations. (4) Once the iterative process was complete, the classification maps contained many polygons representing CRR infection. Some of the smaller polygons represented actual CRR infection, whereas some were artefacts of the classification procedure. The CRR polygons with areas less than or equal to 4 m^2 were filtered out where they were sparse or merged together where they were dense with ArcInfo GIS software (ESRI Inc., Redlands, CA, USA). About 11% of the field was classified as having CRR (Fig. 13.1b) at this point in the classification process, and it occurred at various locations around the field. (5) Ground observations were made to verify that field areas classified as CRR were related to CRR. In general, ground observations supported the classification of field areas into CRR zones based on analysis of the satellite imagery. However, some field areas classified as CRR were related to anomalies such as planter skips and human-caused artefacts that needed to be removed manually from the prescription map. (6) To account for possible spatial variation of CRR from year to year, a buffer of 10 m was added around the CRR areas on the classification map to become part of the treatment area in the prescription map (Fig. 13.1c). The buffer zones significantly increased the treatment area and tended to connect some of the CRR areas, making the prescription map more practical for site-specific application. After this step about 37% of the field was prescribed as treatment area. (7) The polygons in the prescription map were assigned as Spray for CRR areas and No-Spray for non-CRR areas. (8) The prescription map was converted to an ESRI shapefile for use by the variable-rate (VR) application equipment.

The prescription map described in the previous paragraph and based on 2009 satellite data was loaded onto a tractor's VR control system to apply Topguard Terra at planting in 2016. The map was converted to the appropriate format for the variable-rate (VR) control system installed on a John Deere 8230 tractor (Deere & Company, Moline, IL, USA) owned by the cotton grower. Planting of half the field occurred on March 18, 2016 and the other half on March 23. The application rate of Topguard Terra was 0.585 L ha^{-1} (full prescribed rate) mixed with 56.1 L ha^{-1} of water. The liquid was applied during planting with the modified in-furrow method. Liquid flow was distributed to the shanks of a 12-row planter with row spacing at 0.965 m. Rainfall occurred a day after the first half of the field was planted resulting in a poor stand, replanting of that half of the field was required on April 6. No fungicide was applied at replanting.

Two tasks were carried out to evaluate the results of the satellite-based prescription map and VR fungicide application. (A) An as-applied map for the fungicide was recorded during planting (Fig. 13.1d), and it consisted of rectangular regions with fixed width equivalent to the effective swath of the planter (11.58 m). The map data included target and actual rates for comparison between actual application and the prescription. The application system missed some small areas and did not turn on and off exactly when entering and exiting treatment zones, respectively. The actual treatment area was 6% smaller than the prescribed area, and the actual application rate was 0.4% higher than the prescribed rate, but with such small deviations from the prescription map, the VR application was considered adequate for evaluation of overall efficacy. (B) A two-camera aerial imaging system on a manned aircraft, capturing RGB plus NIR images, was used in 2016 to collect post-application images to evaluate the efficacy of the site-specific fungicide application. An image acquired late in the season at 1220 m above ground level (AGL) with a pixel size of 0.30 m was used to detect CRR areas and assess the efficacy of the site-specific application. Compared to the map of fungicide-application zones based on the 2009 image (Fig. 13.1e), the 2016 image (Fig. 13.1f) made it clear that the fungicide effectively controlled the disease in the treated areas, although CRR appeared in a few treated areas towards the end of the growing season. This late CRR manifestation had little effect on yield, because most cotton bolls were fully developed by that time.

13.2.2.2 Manned Aircraft Remote Sensing

High-resolution satellite imagery has shown potential for CRR detection and creating fungicide prescription maps, but manned-aircraft images have been used repeatedly for this purpose on numerous fields (Yang et al. 2014). Aerial imagery has advantages over satellite imagery including higher spatial resolution, more flexibility in timing of data acquisition and the ability to collect data on cloudy days. Yang et al. (2018) used a four-camera system (Yang 2012) to collect RGB plus NIR images of two fields with a history of CRR in different cotton-growing regions of Texas. Field 1 was in southern Texas, and Field 2 was in western Texas. Images were collected from a single-engine aircraft shortly before harvest-to aid application in 2010, when CRR was fully expressed for the season. Image acquisition occurred at 2740 m AGL, giving a pixel resolution of 0.90 m, which was resampled to 1 m.

Prescription maps based on the aerial images of Fields 1 and 2 were created in eight steps, similar to those described in the section on satellite remote sensing. Minor differences are noted here. After step (4), about 33% of Field 1 and 37% of Field 2 were classified as CRR area. In step (6) a 5-m buffer (instead of 10-m) was added around the CRR areas on the classification maps to become part of the treatment area in the prescription maps. After this step about 57% of Field 1 and 63% of Field 2 were prescribed as treatment areas.

These prescription maps based on 2010 aerial image data were loaded onto tractors' variable-rate (VR) control systems to apply fungicide at planting in 2015, the next growing season when access to the field was possible and when cotton was being grown in the rotation. For Field 1 a John Deere VR control system was installed on a John Deere 8230 tractor owned by the grower. Topguard Terra fungicide was applied at planting on May 1, 2015, about six weeks later than the usual planting date because of excessive rainfall. The application rate was 0.292 L ha^{-1} of product (half the prescribed rate) mixed with 56.1 L ha^{-1} of water. Liquid flow was distributed to the shanks of a 12-row planter with row spacing of 0.965 m and applied with the modified in-furrow method. For Field 2 a Trimble Field-IQ spray control system was installed on a John Deere 8210 tractor owned by the grower. The older Topguard fungicide formulation (approved under EPA Section 18) was applied at planting on June 3, 2015. The application rate was 2.34 L ha^{-1} of product (full prescribed rate) mixed with 46.8 L ha^{-1} of water. Liquid flow was distributed to the shanks of an 8-row planter with row spacing of 1.016 m and applied with the T-band method.

Similar to the assessment with satellite imagery, two tasks were carried out to evaluate the results of the aerial-image based prescription map and VR fungicide application. Minor differences are noted here. In task (A), evaluation of an as-applied maps the effective swaths of the planters were 11.58 m in Field 1 and 8.128 m for field 2. The actual treatment area was 1.5% smaller than prescribed for Field 1 and 1.4% larger for Field 2. The actual application rate was 4.1% higher than prescribed for Field 1 and 1.5% lower for Field 2. In task (B), evaluation of post-application images, a two-camera aerial imaging system on a manned aircraft was used in 2015 to collect post-application images. The images were acquired late in the growing season at 1070 m AGL with a pixel size of 0.35 m and used to detect CRR areas. These 2015 post-application images were compared to the 2010 prescription maps to determine efficacy. In Field 1, the fungicide applied at half rate was able to control the disease for most of the growing season, but late-season CRR infection may have had negative effects on cotton yield and quality. In Field 2, the fungicide effectively controlled the disease in the treated areas, although CRR occurred at a few treated areas toward the end of the season but had little effect on the crop.

13.2.2.3 UAV Remote Sensing

Unmanned aerial vehicles (UAVs) have been used extensively for RS in agricultural research over the last few years. While they have disadvantages including large volumes of data and challenges in pre-processing of images, their advantages include higher spatial-resolution imagery, more flexibility in timing of data acquisition and lower cost of data acquisition. With respect to fungicide application for

CRR, technological advances suggest that future VR systems will possibly be capable of precision spraying to the level of an individual seed at planting. For example, state-of-the-art planting systems with real-time kinematic (RTK) Global Navigation Satellite System (GNSS) receivers are currently capable of precisely planting individual seeds at a known location, accurate to within 2 cm, and auxiliary state-of-the-art spraying systems are currently capable of applying starter fertilizer adjacent to each seed planted. The high resolution of UAV imagery, therefore, offers the possibility of prescription maps with extremely high precision, potentially capable of fungicide application on a seed-by-seed basis during planting, and limiting fungicide application to a small area adjacent to each seed planted in a small CRR zone. Research with UAVs for CRR detection was undertaken first to replicate the generation of prescription maps possible with imagery from manned aircraft and satellites, and second to pursue development of prescription maps at the single-plant level. One study (Thomasson et al. 2018) was conducted on a 32.9-ha field in central Texas with a history of CRR. On August 22, 2015, image data in the green, red and NIR bands were acquired with a Lancaster (PrecisionHawk Corp., Raleigh, NC, USA) fixed-wing UAV flown at 120 m AGL, giving 3.7-cm pixels. Another study (Wang and Thomasson 2019) was conducted on a 5.7-ha field with a history of CRR, also in central Texas. In this study RGB plus NIR and red edge band image data were acquired on August 20, 2017, with a UAV Mapper fixed-wing UAV (Tuffwing LLC, Boerne, TX, USA) flown at 120 m AGL, giving 7.6-cm pixels. Images in both studies were acquired with a minimum of 70% image overlap (forward and sideward) to enable generation of a high-quality mosaic.

13.2.2.4 Regional Classification

The methods used previously to classify satellite and manned-aircraft images for CRR have been regional methods, classifying fields into zones of multiple square metres to match the precision of current VR equipment. Regional classification can be based on traditional image-analysis techniques and is relatively computationally efficient. To show the capability of UAVs for practical RS tasks, regional classification of UAV imagery was used to develop CRR prescription maps to demonstrate efficacy, in essence mimicking what has been done previously with manned-aircraft and satellite RS. An image mosaic of the 2015 images of the 32.9-ha field was created with Pix4D software (Lausanne, Switzerland) and resampled in ENVI software (Harris Geospatial, Boulder, CO, USA) to a resolution of 1.0 m per pixel. Support vector machine (SVM) classification was applied to the mosaic to classify it into CRR and non-CRR areas. Based on the classified image data, prescription maps were developed in ArcGIS (ESRI, Redlands, CA, USA). The proportion of CRR area was 5.52% at this stage in the classification process. Ground observations were made to verify CRR areas of various sizes along the western edge and in the southeastern corner of the field, and that the classified CRR areas were actually CRR. In general, most were classified correctly, but a few small areas were misclassified because of, for example, planter skips. To accommodate the potential expansion and temporal variation of the disease, a 5-m buffer zone was created around the infected areas as part of the treatment areas in the prescription map.

The 2015 UAV images were used for VR fungicide application in 2017. The classified image was converted into a shapefile-based prescription map in ArcMap (ESRI, Redlands, CA, USA). The polygons in the prescription map were assigned Spray for CRR areas and No-Spray for non-CRR areas. A Trimble Field IQ system was integrated with a Trimble FM 1000 monitor and a Trimble RTK GNSS receiver installed on a CASE IH Puma 210 Tractor owned by the grower. At planting on April 25, 2017, Topguard Terra was applied with the T-band method at a rate of 0.585 L ha^{-1} (full prescribed rate) with 57.1 L ha-1 of water from a 12-row planter with row spacing of 0.762 m.

An as-applied map (A) was not evaluated in this study, but based on the work with satellite and manned-aircraft imagery the fungicide application was expected to conform closely to the prescription map. Similar to the assessment with satellite and manned-aircraft imagery, one additional task (B) was carried out to evaluate the results of the UAV-based prescription map and VR fungicide application. The UAV images of the 32.9-ha field were collected to determine the efficacy of the UAV-based prescription map based on regional classification. On August 20, 2017, RGB plus NIR and red edge image data were acquired with a Micasense RedEdge camera on a UAV Mapper flown at 120 m AGL, giving 7.64-cm pixel resolution. As with the 2015 image data, the 2017 images were collected with minimum 70% image overlap (forward and sideward) so that a mosaic could be created with Pix4D and processed and classified into CRR and non-CRR areas. These 2017 post-application images were compared to the 2015 prescription maps to determine efficacy. The proportion of CRR area in the field was reduced from 5.52% in 2015 to 0.55% in 2017, giving a strong indication of the efficacy of the UAV-based prescription map in mitigating CRR, similar to the results with manned-aircraft and satellite imagery.

13.2.2.5 Plant-by-Plant Classification

In the future it may be desirable to apply fungicide precisely at a greater level of detail than 5 × 5 m, potentially even at the single-plant level. To take full advantage of the capability of UAV remote sensing, one must utilise the high resolution inherent in the images. Two methods have been developed to approach plant-by-plant (PBP) classification. The first method, a custom row-searching algorithm, identified individual crop rows and then scanned each row, applying a plant-size mask to the image data, to enable PBP classification. A global (i.e. to be used consistently across an entire mosaic) algorithm was developed to exploit the fact that straight rows in a field share the same angle between row direction and latitude lines, so that angles need be measured at only one representative location in a given field. The algorithm automatically pre-processed the mosaic and then measured the row angle based on two-dimensional gradients. Then a morphological operation, tailored to the angle of the rows was used with a customised structural element set to the specific row spacing in the field. Row centre lines were constructed with this process, and then collinear rows were connected across breaks resulting from the presence of long planting skips or streaks of dead plants along the rows. The complete row centre lines were then overlaid onto an image mosaic. Plant-size zones were classified into three categories (live plant, dead plant, and no plant) by applying a plant-size mask from one end to the other on each row. The row-searching algorithm was applied to the mosaic of the 2017 image data from the 32.9-ha field (Fig. 13.2a) and performed well, providing generally accurate identification of live and dead plants. The algorithm was efficient when it was restricted to searching for linear crop rows, requiring only a few minutes of processing on a PC for the entire field. Computation time with curved rows (e.g. in fields irrigated by centre pivot) would probably be significantly longer, and programming improvements would be needed to achieve acceptable processing times.

The second method for PBP CRR classification, a superpixel algorithm, used simple linear iterative cluster (SLIC) superpixel segmentation, a state-of-the-art object-based image classification technique. The superpixel algorithm was applied to the 2015 image mosaic of the 5.7-ha field and 'seeded' (i.e. the iteration process was initiated) with a large number that closely resembled the number of plants expected to be in the field based on planting density. The image of the field was segmented into roughly that number of small pieces (superpixels), each based on the colour, shape and texture of the original image data, and assigned spectral and spatial statistics based on the constituent pixels. The *k*-means clustering was applied automatically to the superpixel image to generate a classification map. The overall algorithm was efficient, taking about two minutes for the 5.7-ha field. The superpixel algorithm provided accurate classification (93.5%) of individual plant zones (Fig. 13.2b), with small errors of omission and commission, and it was faster than the more detailed row-searching algorithm.

13.3 Conclusions

In summary, remote sensing has proved to be useful for developing prescription maps to enable precision application of fungicide to protect cotton plants against CRR disease. High-resolution satellite and manned-aircraft images have been shown to be useful for delineating zones of disease incidence in fields. Images from UAVs can also be used for this purpose, but the extremely high resolution of UAV images also allows for the possibility of plant-by-plant fungicide application. Two studies have shown how individual cotton plants can be located and classified into diseased and healthy categories. Therefore, fungicide applied during planting may, in the future, be placed very precisely next to the seed, further reducing cost and environmental risk associated with over-application.

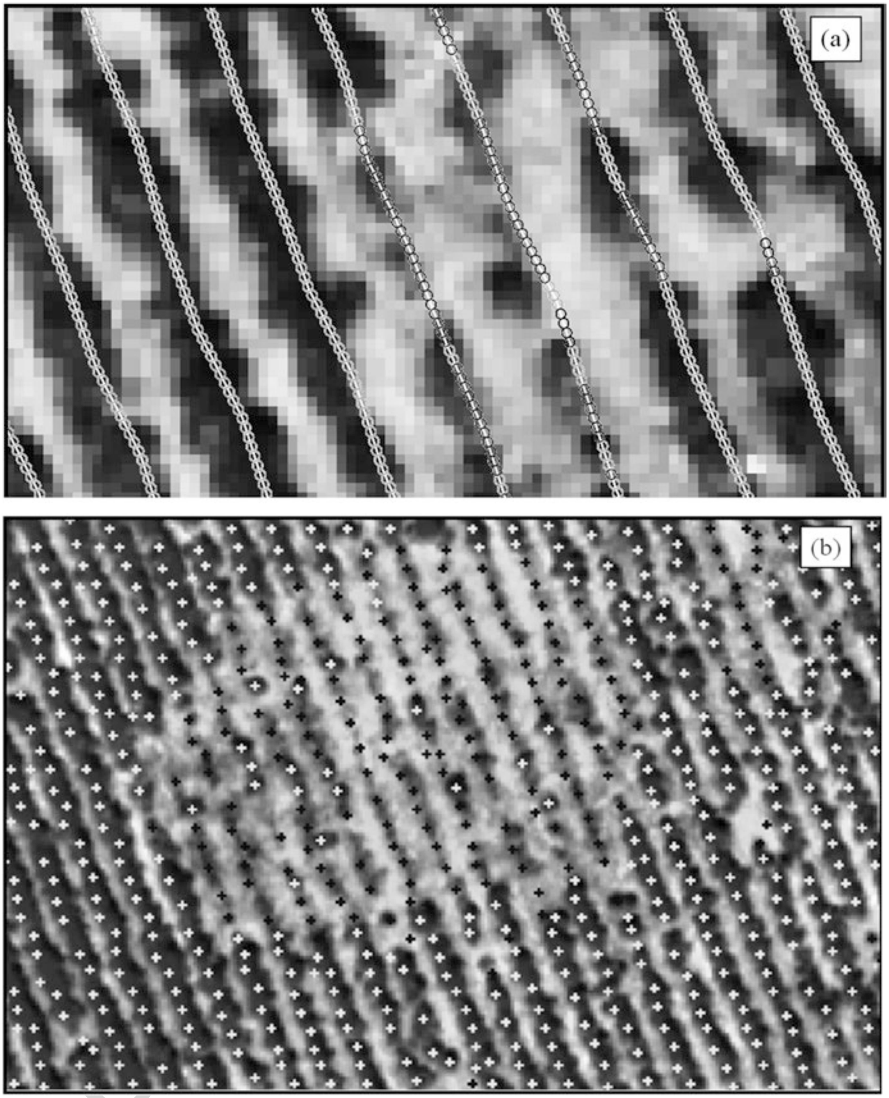

Fig. 13.2 (**a**) Plant-by-plant labelling of live plants (white circles) and dead plants (black circles) and soil (light grey) along cotton rows based on a custom row-searching algorithm. Centre lines of rows recognised by the algorithm are marked with white lines. (**b**) Plant-by-plant labelling of live plants (white crosses) and dead plants (black crosses) based on superpixel classification

13.4 Case Study 13.2. Detection of Laurel Wilt Disease in Avocado: A Case Study for Avocado Production in Florida

13.4.1 Introduction

Avocado (*Persea americana*) is important to the agricultural economy of Florida. The avocado industry is second in importance after citrus; it represents approximately 60% of the tropical fruit crop in Florida (2800 ha) (Evans et al. 2015). It provides an economic benefit of approximately $100 million per year (Evans et al. 2015). In addition, this economic importance reflects that the United States is one of the main producers and importers of avocados in the world (Statista 2018).

However, the avocado industry in Florida is under severe threat because of the invasion of an exogenous pathogen, the Asian fungus *Raffaelea lauricola*, and its original vector, the redbay ambrosia beetle *Xyleborus glabratus*, which causes the lethal vascular disease laurel wilt (Lw) (Ploetz et al. 2011). This complex disease has spread rapidly along the southeastern seaboard of the United States because of the natural dissemination of *X. glabratus*, the great susceptibility of the native *Persea* spp. and their attractiveness to *X. glabratus,* the substantial amounts of inoculum that most females of *X. glabratus* carry and the human transport of infested wood (Hanula et al. 2008; Ploetz et al. 2017a). Moreover, the disease appears to spread through interconnected root systems, which allows the movement of the pathogen without the aid of vectors (Ploetz et al. 2017b). Consequently, Lw has caused the loss of 300 million redbay trees throughout the coastal forests from North Carolina to Florida and over 25,000 avocado trees since its migration into Florida (Ploetz et al. 2017b; Mendel et al. 2018). Furthermore, it is difficult to prevent the spread of the disease as there is no effective fungicide-based control strategy. Sanitation, which consists of identifying affected trees and destroying them before new generations of vectors emerge and colonise new host trees, is the only available control measure (Ploetz et al. 2011; De Castro et al. 2015b).

Laurel wilt impairs xylem function as soon as three days after inoculation, impeding the flow of water and nutrients into affected trees, which soon causes external symptoms of wilting and foliar necrosis in affected portions of the tree, and full defoliation within 2–3 months of symptomatic onset (Ploetz et al. 2011). Before the appearance of external symptoms consisting of leaves changing from an oily green to brown colour, internal symptoms of increased tree temperature that arise from water and nutrient blockage occur. This results in a reduced amount of chlorophyll in the leaves and damaged cell structure (De Castro et al. 2015b). Those variations in leaf plant pigment and temperature make it possible to detect diseased trees, even in the early stages of disease development, with remote sensing tools including those that are spectroscopic and imaging-based.

Laurel wilt symptoms are very similar to those caused by other vascular diseases or factors such as frost damage, Phytophthora root rot, Verticillium wilt, nutrient deficiencies, salinity and fruit stress (overbearing), and consequently their visual discrimination is very difficult (De Castro et al. 2015b). Despite this, diagnostic practice consists of visual inspection of suspect trees, collection of wood and laboratory analyses, which is time-consuming, labour intensive, expensive and requires symptomatic trees. Once plants display external symptoms, it is then complicated to manage the disease because by that time significant colonization of the host by the fungus has already occurred; at which point the best choice is sanitation, i.e. elimination of affected trees (Ploetz et al. 2011). Therefore, a methodology to detect Lw before the external symptoms appears, i.e. at an early stage, and its discrimination from other biotic and abiotic stress factors is highly desirable. This case study describes the required spatial and spectral properties for the rapid and accurate diagnosis of Lw at an early stage using remote sensing tools, long recognised as suitable for the fast monitoring of large areas and reducing the costs of extensive field campaigns. In addition, another widespread avocado disease (Phytophthora root rot caused by *P. cinnamomi*) as well as abiotic factors (salinity and nitrogen and iron nutrient deficiencies), which cause similar symptoms, were evaluated.

13.4.2 Materials and Methods

An effective mapping system begins with an evaluation of the spectral signature at the leaf level of diseases and factors affecting avocado. Once a suitable sensor is selected based on spectral requirements, the study should be scaled up to the canopy level to evaluate other aspects related to image analysis, such as flight altitude, spatial resolution, pre-processing and image algorithm.

13.4.3 Spectral Requirements: Spectral Data Analysis

First, the feasibility of discriminating healthy plants from damaged plants due to biotic and abiotic stressors at an early stage with spectral information was determined. Next, the optimal wavebands and hence the sensor for affected and healthy plant discrimination was selected.

Multivariate analysis tools are considered as one of the most suitable and advanced techniques for the detection of spectral difference (De Castro et al. 2012). Among these tools, neural networks have received great attention from the remote sensing community because of their flexibility and adaptability to the results, tolerance of noisy data and errors, fast computation processing speed, and ability to explore correlations or models that could not be detected by traditional statistical procedures (Han et al. 2012).

13.4.3.1 Spectral Data Collection

Spectral data were taken from avocado leaves under controlled laboratory conditions using a handheld spectroradiometer (SVC HR-1024, Spectra Vista Corp., Poughkeepsie, NY, USA) placed at a height of 50 cm above the leaf. Five reflectance spectra per leaf were taken at the range of 400 to 950 nm with a 10 nm spectral resolution based on published recommendations and the noise of the remainder of the spectral range (Fig. 13.3).

Four asymptomatic and slightly affected leaves in the early stage of stress development, i.e. just beginning to lose turgidity, were selected from each abiotic factor- and disease-affected plant. These leaves were taken from potted ‘Simmonds’ variety avocado trees grown in a greenhouse at the University of Florida’s Tropical Research and Education Center (TREC) in Homestead, FL, USA. The experiment consisted of 10 plants for each class, and all showed symptoms like those caused by Lw. In addition, healthy (H) leaves were obtained from potted plants grown in full sun. The disease induction and symptom development were performed as follows:

- Laurel wilt (Lw): Conidial suspensions of *R. lauricola* with a concentration of 30,000 colony forming units (CFUs) mL^{-1} were introduced in four small holes 5 cm above the soil level around each trunk circumference, resulting in a total of 3000 CFUs per plant. Early symptoms of Lw began to develop by 14 days after inoculation.
- Phytophthora root rot (Prr): 6 g of wheat seed colonised with *P. cinnamomi* were used for the inoculation. Early symptoms, i.e. yellowing of some leaves, appeared after 14 days.

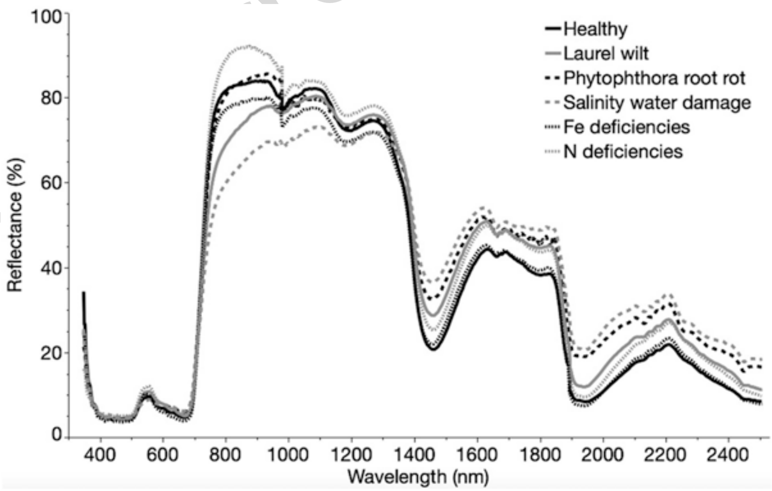

Fig. 13.3 Mean reflectance spectra of leaves representing healthy, laurel wilt, Phytophthora root rot, salinity, water damage, and Fe and N deficiencies of avocado trees. All leaves are typical of the early stage of symptom development. (The figure has been adapted from De Castro et al. 2015a and Abdurhina et al. 2018)

- Salinity (Sln): One litre of a salt solution with a similar concentration to that of sea water from the east coast of Florida, i.e. 36 g L^{-1}, was applied to each tree. Early browning symptoms were found in leaves after seven days.
- Nitrogen (N) deficiency: avocado plants growing in a nutrient-free matrix composed of sand and perlite received a modified Hoagland solution with all essential nutrients except N once a week. Early symptoms occurred 60 days after the beginning of the procedure.
- Iron (Fe) deficiency: these avocado samples grew under the same conditions as N deficient samples, although the applied Hoagland solution contained all the minerals with the exception of Fe. The first symptoms occurred in the same time as the previous case.

The spectral dataset was calibrated using a barium sulphate standard reflectance panel (Spectralon®, Labsphere Inc., North Sutton, NH, USA) in the presence of two portable 500-W halogen work lamps used as extra light source.

13.4.3.2 Spectral Data Analysis

The 10-nm averaged spectral measurements were analysed statistically with the multilayer perceptron (MLP) neural network to identify the best waveband for discrimination of H, Lw and other stressors such as Prr, salinity, and N and Fe deficiencies.

As a multilayer feed-forward neural network, MLP creates an analytically adjusted model based on supervised training with a back-propagation algorithm that minimises the prediction error (Han et al. 2012). The weight, bias and typology parameters of the network are adjusted by learning the relation between inputs (spectral information in this case) and outputs data (health status class in this case). The MLP comprises an input layer, in this case a 10-nm averaged spectral data set, a hidden layer of neurons to compute the data and create the model, and an output layer consisting of the classes to which the samples are classified (H, Lw, and other disease or abiotic factors). The validation of the MLP algorithm was performed by a hold-out cross-validation procedure, where $3n/4$ of the full data set was used to train the model and $n/4$ was used as a test set to provide the generalization accuracy; n was the number of units in the full dataset in every analysis.

The statistical analyses were performed using SPSS software (IBM Statistical Package for Social Science, SPSS Inc., Microsoft Corp., Redmond, WA).

13.4.4 Image Specifications: Image Data Analysis

Multispectral image acquisition and spatial requirements. A user-configurable bandpass filter camera was selected for the experiment. The Tetracam mini-MCA-6 (Tetracam, Inc., Chatsworth, CA, USA) multispectral camera is a lightweight sensor of six individual digital channels with independent optics, each holding a 1.3-megapixel CMOS sensor (1280 × 1024 pixels) with a focal length of 9.6 mm and FOV of 43.7° × 35.6°. Each unit independently stored the data in compact flash cards embedded in the camera. The images were taken in the presence of avocado experts from the Florida Avocado Committee in a commercial avocado production field in Miami-Dade County containing healthy and Lw-infested trees. Experts identified diseased trees that were shortly after confirmed as such by a diagnostic DNA test. No other damaging biotic agents or disturbances were found in or around this field.

The remote images were acquired by a helicopter flight at a height of 250 m, considered to be the optimum height according to the size of typical avocado trees. The pixel size obtained using this sensor at this flight height was 15-cm, large enough to identify a standard avocado tree with a canopy diameter of 7–9 m. Moreover, the average avocado orchard size ranges from 0.4 and 2 ha (Evans et al. 2015), which was covered by images taken with the MCA-camera from a height of 170 m. A lower flight altitude would involve more flight time and cost, and may require an extra mosaicking process to cover the entire field.

Ground truth data. Healthy and Lw avocado trees at early stage were located in the images and manual digitalization was conducted to extract the digital information of the affected portion of the trees and healthy plants. The ground truth data consisted of 21 Lw-infested and 12 healthy trees.

13.4.5 Results

13.4.5.1 Spectral Analysis-Leaf Level

The six channels of the Mini-MCA were selected according to the results obtained in the spectral analysis (Table 13.1), where values ranging from 96% to 100% accuracy were obtained in all the classifications. Table 13.1 shows the wavelengths that contributed to the greater specific weights in the neural network algorithm, which all used one hidden layer with a similar number of neurons.

The most frequently selected 10 nm wavelengths were 740 nm and 750 nm, which were also among the first variables entered into the MLP model in all the cases, indicating that they are crucial in discriminating between infested and healthy avocado plants. An extra filter was selected in the red edge region (760 nm) because wavelengths around that value were chosen in several MLP algorithms and also the importance of that part of the spectrum to detect vascular diseases in plants (De Castro et al. 2015b). The Lw plugs the xylem, blocking the flow of water and increasing the tree temperature. Consequently, leaf chlorophyll concentration and photosynthesis decrease while carotenoid production increases, affecting the reflectance values in the green, red edge and near-infrared regions (Chappelle et al. 1992). For these reasons, it was appropriate to add a filter in the NIR region. Taking into account the most frequently selected wavelengths in that part of the region,

Table 13.1 Accuracy assessment on 10-nm bandwidth data classification for healthy (H), laurel wilt-infested plants (Lw) and other stressors such as Phytophthora root rot (Prr), salinity (Sln) and N and Fe deficiencies, using MLP neural networks

Analysed classes	Selected wavelengths[a] (nm)	Accuracy (%)
H *vs* Lw *vs* Prr	740, 750, 830, 760	100
H *vs* Lw *vs* N vs Fe	840, 930, 750, 720, 830, 740	100
H *vs* Lw *vs* Sln	720, 750, 740, 526, 950, 770	96

[a]Wavelengths selected to account for the greater specific weights in the neural network algorithm

economic reasons and commercial availability, a band with a centre wavelength at 850 nm and 40 nm full-width was added to the camera. In addition, because of those changes in the vegetal pigment concentrations, the absolute difference between the red edge and NIR region with the green one decreases in diseased plant spectral data, making the ratios between bands useful to separate plants affected by damaging agents from healthy ones. Therefore, an additional filter was selected in the green region (580–10 nm full-width). Finally, another 10 nm full-width (650 nm) was added in the red region because the large variety of narrow-band vegetation indices (VIs) obtained from remote sensing data to assess plant health rely on the combination of NIR and red reflectance.

13.4.5.2 Image Processing-Canopy Level

After the suitable filters were selected and attached to the camera, images were taken to assess the feasibility to detect infested avocado plants at an early stage of symptom development.

13.4.5.3 Multispectral Band Alignment and Image Radiometric Calibration

Both processing steps are required before image analysis. The alignment process reduces geometric differences between the bands and groups the six images saved in each channel. This was carried out by Tetracam PixelWrench 2 (PW2) software (Tetracam Inc.) that provides a band-to-band registration file. During this process, the vignetting parameters were also adjusted.

Radiometric correction was conducted using two calibration targets (black of 3% and white of 82%) and an empirical line calibration method with ENVI software (ENVI®, Research Systems Inc., Boulder, CO, USA).

13.4.5.4 Image Data Analysis

The mean digital information extracted from pixels of Lw–infested and healthy trees was used to calculate and evaluate a large pool of VIs calculated from the six bands of the customised MCA camera. The VIs have been widely used in physiological stress detection (Lu et al. 2017, 2018) as they magnify the differences in spectral signatures, thus making the identification of infested plants easier (Mahlein et al. 2012).

The *M*-statistic was applied to quantify the histogram separation of vegetation indices and to establish their potential for spectral discrimination. The *M*-statistic evaluates the mean (μ) difference of the class 1 and class 2 histograms normalised by the sum of their standard deviations (σ) (Kaufman and Remer 1994) (Eq. 13.1). The larger is the M value, the better is the spectral separation. Values less than 1 indicate poor separation.

$$M = \frac{\mu_{\text{class1}} - \mu_{\text{class2}}}{\sigma_{\text{a}} + \sigma_{\text{b}}} \quad (13.1)$$

The resulting *M* values varied according to the vegetation indices, suggesting that the separation capacity depends largely on the spectral region analysed. Only *M* values >1.5 were considered as indicators of strong discriminatory power here. The best results were obtained with red edge/G, GRVI, VIgreen and GNDVI, where any of the bands related to the red edge region (740, 750 and 760 nm) of the Tetracam camera were used (Table 13.2). These VIs work by combining digital values in the green, red edge and near-infrared region of the spectrum and are related to changes in vegetal pigment concentration and cellular damage, both of which occur in Lw-infested plants due to xylem blockage. These results confirm the importance of proper band selection early in the procedure because their use made it possible to

Table 13.2 The M values obtained in the analysis of digital data of laurel wilt-infested trees at the early stage of symptom development and those of healthy avocado trees using remote sensed data

Vegetation Index	Equation	Adapted from	Bands used	*M* value
R/G	Redge$_x$/G	–	Redge$_{740}$	1.8
			Redge $_{50}$	1.8
			Redge$_{760}$	2.1
Green ratio vegetation index	GRVI = NIR$_x$/G	–	NIR$_{850}$	1.9
Green vegetation Index	$\text{VIgreen} = \frac{G - R_x}{G + R_x}$	Gitelson et al. 2002	Redge$_{740}$	1.8
			Redge$_{750}$	1.8
			Redge$_{760}$	2.1
Green normalised difference vegetation index	$\text{GNDVI} = \frac{\text{NIR}_x - G}{\text{NIR}_x + G}$	Gitelson et al. 1996	NIR$_{850}$	1.8

Redge$_x$ in this form represents the filters in the red edge region of the MCA-camera used to calculate the VI. i.e., 740, 750 or 760 nm identify Lw-infested trees at an early stage of disease development with minimal symptoms, i.e. leaves are still green and have barely begun to lose turgidity.

Therefore, the analysis of images obtained from the camera with the attached filters using the selected VIs can overcome the challenge of early detection of Lw, which represents a great advance in preventing the spread of this lethal avocado disease.

13.5 Conclusions

The spatial and spectral specifications for the quick and accurate diagnosis of Lw at an early stage, as well as the possibility to separate it from other abiotic and biotic factors that cause similar symptoms, were evaluated in this case study. Therefore, once suitable sensor and flight planning requirements have been defined, an automatic algorithm based on aerial system imaging, such as UAV, may be developed for early and rapid Lw detection in further research. The early detection of LW will prevent the spread of the disease and facilitate the implementation of disease control precision strategies, such as targeted sanitation, in the context of PA.

13.6 Case Study 13.3. The Use of Hyperspectral Imaging for Esca Detection in a Vineyard

13.6.1 Introduction

Hyperspectral (HS) imaging systems are one of the most currently used image-based phenotyping methods in modern agriculture due to their inherent advantages. They include the possibility of acquiring data in a non-destructive and non-invasive way, being amenable to automation and allowing in-field sample analyses (ElMasry and Sun 2010). For these reasons, HS systems represent a promising tool for plant disease diagnosis, together with the fact that not only can an infection be identified successfully, but also its location within the plant can be detected (Mutka and Bart 2015; Rançon et al. 2019). The HS techniques generally work in the near-infrared (NIR) region of the electromagnetic spectrum because the spectral signature of vegetation is characterised by high reflectance in this region (Rodríguez-Pérez et al. 2007). It is particularly relevant for disease detection, as symptoms can sometimes be detected before the naked eye is able to do so (Di Gennaro et al. 2016). Thus, HS systems may have the potential to enable diagnosis of plant diseases that have no visible symptoms at the early stages of their development, as in the case for esca, a grapevine fungal trunk disease.

Currently, grapevine trunk diseases are one of the main concerns of viticulture worldwide because they are responsible for substantial economic loss to the wine industry (Levasseur-Garcia et al. 2016). They result in a decrease in crop productivity and, in many cases, the early decay of plants (Laveau et al. 2009). Among these diseases the most prominent in the Mediterranean countries is esca (Fischer 2002). It was considered to be a problem in older vineyards only, and it was relatively easily controlled with fungicides (Graniti et al. 2000). However, the use of sodium arsenite – the main fungicide tool against it – was banned at the beginning of the twenty-first century in many countries which, together with other changes in growing techniques, led to a considerable increase in esca incidence worldwide (Bertsch et al. 2009).

Esca is a complex disease, mainly caused by the ascomycete fungi *Phaeomoniella chlamydospore* and *Phaeoacremonium aleophilum* and the basidiomycete fungus *Formitiporia mediterranea* (Di Marco et al. 2011). It usually affects adult plants aged above 10 years, either causing foliar discoloration or sudden wilting of the entire vine (apoplexy) which kills the plant within a short period (Mugnai et al. 1999). Affected leaves generally show a 'tiger-stripe' pattern (Surico et al. 2008), while a characteristic spotting, described as 'black measles' in the USA, is observed on berries (Mugnai et al. 1999). Foliar symptoms may or may not be observed in consecutive years, but affected plants generally end up dying from apoplexy (Hofstetter et al. 2012). Currently, in the absence of chemical methods of control of proven efficiency against esca, any treatment should be preventive and various cultural and crop management measures are recommended, including good pruning practices and the use of a high-quality plant material (García-Jiménez et al. 2010). Once the vine is affected, alterations to the cells arise at leaf level before symptoms become visible (Valtaud et al. 2009). Therefore, a technique capable of detecting infected vines before the symptoms become visible would allow better crop management and decision-making.

The present case study shows the potential of a near-infrared hyperspectral system (NIR-HSI) to distinguish between visually asymptomatic grapevine leaves, picked from esca-affected vines, and symptomatic leaves, collected from the same vines, at a laboratory scale. This methodology opens up an area of research aiming to apply it at the field scale through the development of sensors that could help growers to detect disease presence early, before the symptoms become visually noticeable.

13.6.2 Materials and Methods

13.6.2.1 Plant Material

In this study, grapevine leaves of cv. Tempranillo (*Vitis vinifera* L.) picked from an experimental vineyard belonging to the Viticulture and Enology Station of Navarra (EVENA) and located in Olite (Navarra, Spain) were used. Two leaf categories were selected visually, identified and handpicked from the field at a growth stage close to harvest (September 20, 2018). A total of 60 samples were collected: 30

asymptomatic leaves from esca-affected vines, named Esca 1 (E1), and 30 symptomatic leaves from the same esca-affected vines of class E1 and designated Esca 2 (E2). Samples were kept in cold storage at 3 °C until analysis. The measurements were made approximately 24 h later. Before hyperspectral image acquisition, a reference RGB image was obtained for each leaf.

13.6.2.2 Hyperspectral Imaging

Hyperspectral Image Acquisition

Hyperspectral images were recorded using an NIR-HSI system consisting of an NIR InGaAs camera with 320 × 256 pixel resolution (Xeva 1.7–320, Xenics, Leuven, Belgium) coupled to a spectrograph (ImSpector N17E, Specim, Spectral Imaging Ltd., Oulu, Finland), both sensitive in the range 900–1700 nm. This line-scanning imager was mounted 400 mm above a linear translation stage (LEFS25, SMC Corporation, Tokyo, Japan) that allowed samples to be moved under the field of view of the camera. Four 46 W halogen lamps and a black cover enclosing the entire set-up were used for stable lighting conditions of the scene. A computer equipped with Xeneth 2.5 and ACT Controller software was used to control the camera and the translation stage and to record the leaf images.

One hyperspectral image of the adaxial leaf side was acquired per sample with a spatial resolution of 0.75 mm per pixel (320 pixels per line) and a spectral resolution of about 3 nm (256 spectral bands). Detector saturation was avoided by optimizing the integration time at 2 ms. In addition, white reference with standard reflectance of 99% (Teflon white calibration tile, Specim, Spectral Imaging Ltd., Oulu, Finland) and dark reference (camera lens covered by an opaque black cap) images were taken for reflectance calibration.

Image Processing

The first step in image processing consisted of forming the three-dimensional data cube (hypercube) by stacking the raw leaf images. Then, reflectance calibration was performed to convert the raw intensity values in hyperspectral images into relative reflectance (R) values by using Eq. 13.2 (Geladi et al. 2004):

$$R = \frac{I_{\mathrm{Raw}} - D}{\mathrm{W} - \mathrm{D}}, \tag{13.2}$$

where I_{Raw} is the raw irradiance intensity acquired on the sample, D is the intensity acquired for the dark reference and W is the intensity acquired on the white reference.

At the next step, images were segmented to separate the region of interest, in this case the whole leaf, from the saturated areas and background. In this study segmentation was accomplished following the algorithm presented in Lopez-Molina et al.

(2017). Moreover, data between 900–1000 nm were removed as spectral noise was observed within that region.

Finally, the relevant spectral data were extracted by unfolding the 3-dimensional hypercube into a 2-dimensional data matrix of the leaf pixel reflectance values at the selected wavelengths (224 bands). In this case, the dataset was divided randomly into calibration and validation groups, comprising 60 and 40% leaves of each class, respectively. For each leaf that composed the calibration group (18 images per class), 10 pixels were manually selected using the graphical user-friendly interface HYPER-Tools (Mobaraki and Amigo 2018) and taking the RGB images as a reference. For class E1, pixels were selected from one external and one internal leaf ring (5 pixels per ring), while for class E2 only the pixels corresponding to leaf zones with visible esca symptoms were selected. The resulting X matrix consisted of 360 rows and 224 columns (180 rows per class), and was used as the calibration set to form classification models. In the remaining 12 images per class, the unfolding process was performed automatically, and one matrix including the leaf pixels contained in the segmented mask was obtained for each leaf sample for validation purposes.

Image processing was performed in MATLAB R2016b (The MathWorks, Natick, MA, USA).

13.6.2.3 Multivariate Data Analysis

Data processing and qualitative analysis were performed using the PLS_Toolbox (Eigenvector Research Inc., Wenatchee, WA) within MATLAB® computational environment.

Spectral Pre-processing

Prior to model building, spectral data were pre-processed to correct light scattering and system noise effects. The following pre-processing techniques were tested individually and combined: standard normal variate (SNV), multiplicative scatter correction (MSC), detrending, smoothing, and first and second derivatives (1st Der and 2nd Der, respectively). Smoothing was performed using the Savitzky–Golay algorithm, on a total window of 15 points and a zero-order polynomial, while derivatives were calculated using the Savitzky–Golay method by second order polynomial and a 15-point window. The effect of no pre-processing (None) was also analysed.

Leaf Pixel Classification

A partial least squares discriminant analysis (PLS-DA) method was used to create a two-class classifier to differentiate pixels belonging to class E1 (asymptomatic leaves from esca-affected vines) from those belonging to class E2 (symptomatic leaves). The PLS-DA is a supervised classification technique in which a PLS regression is carried out to predict class membership (Barker and Rayens 2003). For that reason, a **Y** matrix consisting of 0 s and 1 s needs to be formulated to indicate class membership (1) or non-membership (0). In this case, the spectral information (**X** matrix) was linked with the category the samples belonged to (E1 or E2) (**Y** matrix).

As stated above, 60% of samples (36 leaves) of each class were randomly selected for calibration and cross-validation (CV; Venetian blinds cross-validation method with 10 data splits), while the remaining 40% (24 leaves) were used as a validation group.

The performance of PLS-DA models was evaluated in terms of the percentage of correctly classified (%CC) pixels, and the sensitivity and specificity in CV, together with the percentage of correctly predicted pixels per class obtained on each sample in the validation.

13.6.3 Results and Discussion

Figure 13.4 shows the mean spectra of the selected pixels of each of the two classes, E1 (asymptomatic) and E2 (symptomatic), in the calibration group. Considerable differences in the magnitude of reflectance were observed between the two classes along the selected spectral range (1000–1700 nm). A deep dip in the spectrum is

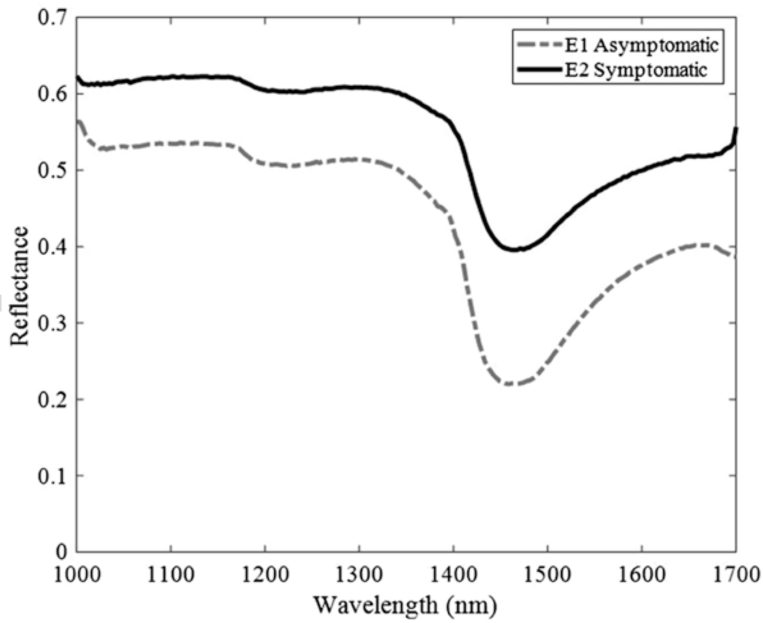

Fig. 13.4 Mean spectra of classes E1 and E2 in the calibration group

evident at around 1450 nm because of the first overtone of the OH-stretching band (Osborne et al. 1993). As can be seen in Fig. 13.4 the reflectance of class E1 at 1450 nm is lower and thus, absorbance was higher, than that of class E2. Since the strong water absorption bands near this wavelength change according to the water content status of foods (Büning-Pfaue 2003), it is hypothesised that this difference occurs because of the greater water content in the asymptomatic leaves than symptomatic ones where esca has already caused desiccation of some leaf areas. This statement accords with the findings of Büning-Pfaue (2003), who observed that the absorption band at around 1400 nm of sliced pear flesh decreased in intensity at the same time as dehydration increased.

Table 13.3 presents the % CC pixels in the calibration and the CV groups obtained with the different pre-processing methods applied. The number of samples (*n*) (after elimination of outliers) and the number of latent variables (LVs) used to develop the PLS-DA models are also included. Good classification results were obtained with all of the pre-processing techniques, achieving more than 85% CC pixels. However, the best results were achieved when applying smoothing, with more than 94% of pixels correctly classified in the CV group.

Table 13.4 shows the confusion matrix and the sensitivity and specificity values obtained for the CV group after the smoothing pre-process. Class E1 has a higher sensitivity value than class E2, indicating that pixels belonging to E1 were classified better into their corresponding group (97.2% CC *versus* 92.2%).

Table 13.3 Number of LVs and % CC samples obtained in the PLS-DA models with the different pre-processing

Pre-processing	*n*	LVs	% CC_{Cal}	% CC_{CV}
None	360	3	91.9	91.1
SNV	354	3	91.0	90.4
MSC (mean)	358	2	90.8	90.5
Detrending	360	2	90.8	89.7
Smoothing	360	5	**95.3**	**94.7**
1st Der	360	4	90.6	90.6
2nd Der	358	3	86.6	85.2
Smoothing+2nd Der	360	3	89.7	88.6
Smoothing+MSC	360	4	90.6	90.0
Smoothing+SNV	358	4	90.5	89.9
Smoothing+1st Der	360	2	89.7	90.0
1st Der + MSC	359	6	93.6	93.0
1st Der + SNV	360	4	90.8	90.6

Values in bold correspond to the highest % CC pixels in the PLS-DA models

Table 13.4 Confusion matrix and sensitivity and specificity values of CV group after smoothing

		Actual class (%)		Sensitivity	Specificity
Predicted class (%)	E1	97.2	7.8	0.972	0.928
	E2	2.8	92.2	0.928	0.972
	Not assigned	0	0		

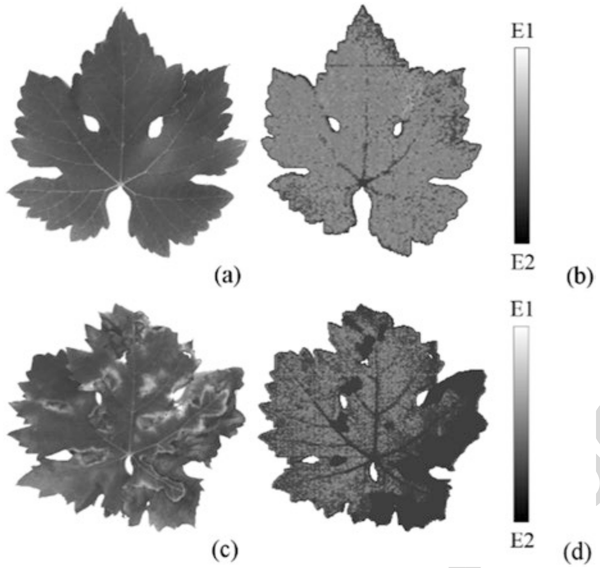

Fig. 13.5 Classification of pixels in the validation (grey: E1 class; black: E2 class) leaf samples (**a**,**b**) E1; (**c**,**d**) E2 obtained by HS system (b,d) and their corresponding RGB images (a,c)

This is an interesting result, since quite the opposite was expected, i.e. that symptomatic pixels would have been classified better than asymptomatic ones. However, this highlights the capability of HS systems to identify vines potentially affected by esca, but without visual symptoms.

Regarding the results obtained for the validation group (24 leaves) (data not shown), in most cases, a larger proportion of pixels was classified into the class they belong to. In total, 84% of the pixels from the 12 leaves of class E1 were correctly classified into their corresponding class (asymptomatic), whereas 76% of the pixels from the 12 leaves of class E2 were correctly labelled as symptomatic.

Figure13.5 displays the classification of pixels from two leaves of the validation group belonging to classes E1 (a,b) and E2 (c,d), respectively. Images in Fig. 13.5a and c correspond to the RGB images taken as reference and images in Fig. 13.5b and d are those obtained by the HS system. In sample E1 (Fig. 13.5b) 77.5% of pixels were correctly assigned as class E1 (grey pixels), whereas in sample E2 (Fig. 13.5d) 76.8% of pixels were classified as class E2 (black pixels). Fig. 13.5d also shows that most of the black pixels were at the edges of the leaf, matching the most esca-affected areas as shown in the equivalent RGB image (Fig. 13.5c).

13.7 Conclusions

The feasibility of NIR hyperspectral imaging, combined with multivariate analysis, to differentiate between asymptomatic and symptomatic leaves from esca-affected vines was evaluated in this case study. Good classification rates (above 85% CC in

CV) were obtained when applying different pre-processing techniques in PLS-DA models. More accurate discrimination of asymptomatic (E1) and symptomatic (E2) pixels was achieved after the smoothing pre-process (94.7% CC). Furthermore, a pixel-based prediction accuracy above 75% was obtained in the validation group. Class E1 was classified better than class E2 suggesting that HS systems could be used for esca diagnosis at early stages of infection.

13.8 Conclusions for the Chapter

Based on the importance of having early and accurate indicators of disease infestation in crops for timely and proper disease control management, case studies in cotton, avocado and grape vines using remote sensing technology have been illustrated. Different acquisition platforms were evaluated, such as leaf-level hyperspectral data and canopy-level remote imagery taken from manned airplanes or helicopter and UAVs, as well as from satellites. The results proved that remote sensing is very useful, efficient and effective for identifying CRR zones in cotton field, laurel wilt-infested avocado trees and esca-affected vines. The use of powerful analytical algorithms on remotely-sensed data enables the challenge of detecting infested plants at an early stage to be overcome, i.e. with minimal symptoms, discriminating them from asymptomatic plants and from plants affected by other biotic and abiotic factors that cause similar symptoms, and for developing prescription maps. Therefore, the combination of suitable remote-sensing data and advanced algorithms are presented as robust tools for rapid and accurate disease detection, offering major savings compared to traditional diagnostics such as visual inspection, which is costly, time-consuming, and subject to human bias. The choice between the remote-sensing platforms and analysis techniques depends on the agronomic goal, the cost and availability of data and their ease of analysis, the computing power required and the overall ease of use.

The early identification of infested plants could assist growers in the decision-making process and in developing proper and timely site-specific disease management strategies to control the spread of these important diseases. In addition, the use of disease and prescription maps would allow farmers to optimise inputs and field operations, resulting in reduced yield losses and increased profits. Consequently, the environmental impact would be lessened with fewer and targeted inputs. Further research should be aimed at developing automatic algorithms applied at the plant level to control the evolution of these diseases in a robust, fast and accurate way.

Acknowledgments The research presented here was partly financed by the USDA Specialty Block Grant No. 019730 (Florida Department of Agriculture and Consumer Services, USA), AGL2017-83325-C4-1R and AGL2017-83325-C4-4R Projects (Spanish Ministry of Science, Innovation and Universities and AEI/EU-FEDER funds), Public University of Navarre postgraduate scholarships (FPI-UPNA-2017, Res.654/2017), Project DECIVID (Res.104E/2017, Department of Economic Development of the Navarre Government-Spain), and the Spanish MINECO project TIN2016-77356-P (AEI, Feder/UE). The authors thank Don Pyba and Sherrie Buchanon for their helpful assistance, as well as the Viticulture and Enology Station of Navarra-Spain (EVENA) for providing the samples and for their valuable support.

References

Abdulridha J, Ampatzidis Y, Ehsani R, de Castro A (2018) Evaluating the performance of spectral features and multivariate analysis tools to detect laurel wilt disease and nutritional deficiency in avocado. Comput Electron Agric 155:203–211

Barker M, Rayens W (2003) Partial least squares for discrimination. J Chemometr 17(3):166–173

Bertsch C, Larignon P, Farine S et al (2009) The spread of grapevine trunk disease. Science 324(5928):721

Büning-Pfaue H (2003) Analysis of water in food by near infrared spectroscopy. Food Chem 82(1):107–115

Campbell JB (2002) Introduction to remote sensing, 3rd edn. Guilford Press, New York

Chappelle EW, Kim MS, McMurtrey JE (1992) Ratio analysis of reflectance spectra (RARS): an algorithm for the remote estimation of the concentrations of chlorophyll A, chlorophyll B, and carotenoids in soybean leaves. Remote Sens Environ 39(3):239–247

De Castro AI, Jurado-Expósito M, Gómez-Casero MT et al (2012) Applying neural networks to hyperspectral and multispectral field data for discrimination of cruciferous weeds in winter crops. Sci World J 630390

De Castro AI, Ehsani R, Ploetz R et al (2015a) Optimum spectral and geometric parameters for early detection of laurel wilt disease in avocado. Remote Sens Environ 171:33–44

De Castro AI, Ehsani R, Ploetz RC et al (2015b) Detection of laurel wilt disease in avocado using low altitude aerial imaging. PLoS One 10(4):e0124642

Di Gennaro SF, Battiston E, Di Marco S et al (2016) Unmanned Aerial Vehicle (UAV)-based remote sensing to monitor grapevine leaf stripe disease within a vineyard affected by esca complex. Phytopathol Mediterr 55(2):262–275

Di Marco S, Osti F, Calzarano F et al (2011) Effects of grapevine applications of fosetyl-aluminium formulations for downy mildew control on “esca” and associated fungi. Phytopathol Mediterr 50(4):S285–S299

Drake DR, Minzenmayer RR, Multer WL et al (2013) Evaluation of farmer applications of Topguard (flutriafol) for cotton root rot control in the first Section 18 exemption year. In: Proccedings of the Beltwide Cotton Conf. National Cotton Council of America, Cordova

ElMasry G, Sun DW (2010) Principles of hyperspectral imaging technology. In: Sun DW (ed) Hyperspectral imaging for food quality analysis and control. Academic Press, San Diego, pp 3–43

Evans EA, Bernal Lozano I (2015) Sample avocado production costs and profitability analysis for Florida. Electronic data information source (EDIS) FE837. Gainesville, FL: Food and Resource Economics Department, University of Florida. https://edis.ifas.ufl.edu/dosearch.html. Accessed 23 March 2018

Fischer M (2002) A new wood-decaying basidiomycete species associated with esca of grapevine: *Fomitiporia mediterranea* (Hymenochaetales). Mycol Prog 1(3):315–324

García-Jiménez J, Raposo R, Armengol J (2010) Enfermedades fúngicas de la madera de la vid. In: Jiménez-Díaz RM, Montesinos Seguí E (eds) Enfermedades de las plantas causadas por hongos y oomicetos: naturaleza y control integrado. SEF-Phytoma España, pp 161–189

Geladi P, Burger J, Lestander T (2004) Hyperspectral imaging: calibration problems and solutions. Chemom Intell Lab Syst 72(2):209–217

Gitelson AA, Merzlyak MN (1996) Signature analysis of leaf reflectance spectra: algorithm development for remote sensing of chlorophyll. J Plant Physiol 148(3–4):494–500

Gitelson AA, Kaufman YJ, Stark R et al (2002) Novel algorithms for remote estimation of vegetation fraction. Remote Sens EnvironRemote Sens Environ 80(1):76–87

Graniti A, Surico G, Mugnai L (2000) Esca of grapevine: a disease complex or a complex of diseases? Phytopathol Mediterr 39(1):16–20

Han J, Kamber M, Pei J (2012) Data mining. Concepts and techniques, 3rd edn. Morgan Kaufmann Publishers, Waltham

Hanula JL, Mayfield AE III, Fraedrich SW et al (2008) Biology and host associations of redbay ambrosia beetle (*Coleoptera: Curculionidae: Scolytinae*), exotic vector of laurel wilt killing redbay trees in the southeastern United States. J Econ EntomolJ Econ Entomol 101(4):1276–1286

Hofstetter V, Buyck B, Croll D et al (2012) What if esca disease of grapevine were not a fungal disease? Fungal Divers 54:51–67

Howden SM, Soussana JF, Tubiello FN et al (2007) Adapting agriculture to climate change. Procceding of the Natl Acad Sci USA 104(50):19691–19696

Isakeit T, Minzenmayer R, Sansone C (2009) Flutriafol control of cotton root rot caused by Phymatotrichopsis omnivora. In Procceding of the Beltwide Cotton Conf. 130–133. Cordova, Tenn.: National Cotton Council of America

Kaufman YJ, Remer LA (1994) Detection of forests using mid-IR reflectance: an application for aerosol studies. IEEE Trans Geosci Remote Sens 32(3):672–683

Laveau C, Letouze A, Louvet G et al (2009) Differential aggressiveness of fungi implicated in esca and associated diseases of grapevine in France. Phytopathol Mediterr 48(1):32–46

Levasseur-Garcia C, Malaurie H, Mailhac N (2016) An infrared diagnostic system to detect causal agents of grapevine trunk diseases. J Microbiol Methods 131:1–6

Lopez-Molina C, Ayala-Martinez D, Lopez-Maestresalas A et al (2017) Baddeley's Delta metric for local contrast computation in hyperspectral imagery. Prog Artif Intell 6:121–132

Lu JZ, Ehsani R, Shi YY et al (2017) Field detection of anthracnose crown rot in strawberry using spectroscopy technology. Comput Electron Agric 135:289–299

Lu JZ, Ehsani R, Shi YY et al (2018) Detection of multi-tomato leaf diseases (late blight, target and bacterial spots) in different stages by using a spectral-based sensor. Sci Rep 8:2793

Lyda SD (1978) Ecology of *Phymatotrichum omnivorum*. Annu Rev Phytopathol 16:193–209

Mahlein AK (2016) Plant disease detection by imaging sensors – parallels and specific demands for precision agriculture and plant phenotyping. Plant Dis 100(2):241–251

Mahlein AK, Steiner U, Hillnhütter C et al (2012) Hyperspectral imaging for small-scale analysis of symptoms caused by different sugar beet diseases. Plant Methods 8:3

Mendel J, Burns C, Kallifatidis B et al (2018) Agri-dogs: using canines for earlier detection of laurel wilt disease affecting avocado trees in South Florida. HortTechnology 28(2):109–116

Mobaraki N, Amigo JM (2018) HYPER-Tools. A graphical user-friendly interface for hyperspectral image analysis. Chemom Intel Lab Syst 172:174–187

Mugnai L, Graniti A, Surico G (1999) Esca (black measles) and brown wood-streaking: two old and elusive diseases of grapevines. Plant Dis 83(5):404–418

Mutka AM, Bart RS (2015) Image-based phenotyping of plant disease symptoms. Front Plant Sci 5:734

NCC (2013) Disease Database (2011). National Cotton Council of America, Cordova. Available at: http://www.cotton.org/tech/pest/index.cfm. Accessed 20 February 2013

Oerke EC, Dehne HW (2004) Safeguarding production - losses in major crops and the role of crop protection. Crop Prot 23:275–285

Osborne BG, Fearn T, Hindle PH (1993) Practical NIR spectroscopy with applications in food and beverage analysis. Longman Scientific and Technical, Harlow

Pammel LH (1888) Root rot of cotton, or "cotton blight". Texas Agric Exp Station Ann Report 1:50–65

Ploetz RC, Harrington T, Hulcr J et al (2011) Recovery plan for laurel wilt of avocado (caused by *Raffaelea lauricola*). National Plant Disease Recovery System. Homeland Security Presidential Directive Number 9 (HSPD-9). http://www.ars.usda.gov/research/docs.htm?docid=14271 accessed 20 April 2013

Ploetz RC, Konkol JL, Narvaez T et al (2017a) Presence and prevalence of *Raffaelea lauricola*, cause of laurel wilt, in different species of ambrosia beetle in Florida USA. J Econ Entomol 110(2):347–354

Ploetz RC, Kendra PE, Choudhury RA et al (2017b) Laurel wilt in natural and agricultural ecosystems: understanding the drivers and scales of complex pathosystems. Forest 8(2):48

Rançon F, Bombrun L, Keresztes B et al (2019) Comparison of SIFT encoded and deep learning features for the classification and detection of esca disease in Bordeaux vineyards. Remote Sens (Basel) 11(1):1–26

Rodríguez-Pérez JR, Riaño D, Carlisle E et al (2007) Evaluation of hyperspectral reflectance indexes to detect grapevine water status in vineyards. Am J Enol Vitic 58(3):302–317

Smith HE, Elliot FC, Bird LS (1962) Root rot losses of cotton can be reduced. Pub. No. MP361. Texas A&M Agricultural Extension Service, College Station

Statista (2018) Import value of avocados worldwide in 2017, by leading country (in million U.S. dollars). Source: UN Comtrade; 2017. https://www.statista.com/statistics/938571/major-importers-avocado-import-value/ Accessed 06 November 2018

Surico G, Mugnai L, Marchi G (2008) The esca disease complex. In: Ciancio A, Mukerji KG (eds) Integrated management of diseases caused by fungi, phytoplasma and bacteria. Integrated management of plant pests and diseases, vol 3. Springer, Dordrecht, pp 119–136

Thomasson JA, Wang T, Wang X et al (2018) Disease detection and mitigation in a cotton crop with UAV remote sensing. In Proccedings of the autonomous air and ground sensing Systems for Agricultural Optimization and Phenotyping. Bellingham, Wash.: SPIE

Valtaud C, Larignon P, Roblin G et al (2009) Developmental and ultrastructural features of *Phaeomoniella chlamydospora* and *Phaeoacremonium aleophilu*m in relation to xylem degradation in esca disease of the grapevine. J Plant Pathol 91(1):37–51

Wang T, Thomasson JA (2019) Plant-by-plant level classifications of cotton root rot by UAV remote sensing. In Proccedings of the Autonomous Air and Ground Sensing Systems for Agricultural Optimization and Phenotyping. Bellingham, Wash.: SPIE

Yang C (2012) A high-resolution airborne four-camera imaging system for agricultural remote sensing. Comput Electron Agric 88(1):13–24

Yang C, Odvody GN, Fernandez CJ et al (2014) Monitoring cotton root rot progression within a growing season using airborne multispectral imagery. J Cotton Sci 18(1):85–93

Yang C, Odvody GN, Thomasson JA et al (2016) Change detection of cotton root rot infection over 10-year intervals using airborne multispectral imagery. Comput Electron Agric 123(1):154–162

Yang C, Odvody GN, Thomasson JA et al (2018) Site-specific management of cotton root rot using airborne and high-resolution satellite imagery and variable-rate technology. Trans ASABE 61(3):849–858

Zhang J, Huang Y, Pu R et al (2019) Monitoring plant diseases and pests through remote sensing technology: a review. Comput Electron Agric 165:104943

Author Queries

Chapter No.: 13 460279_1_En_13_Chapter

Queries	Details Required	Author's Response
AU1	Please confirm whether the presented affiliations are okay.	
AU2	For the authors ➔ Please amend according to Springer instructions: *Springer directions:* *Each keyword should not contain more than two compound words, and each keyword phrase should start with an uppercase letter. We allow three to six keywords. When selecting the keywords, think of them as terms that will help someone locate your chapter at the top of the search engine list using, for example, Google. Very broad terms, (e.g., "Case study" by itself) should be avoided as these will result in thousands of search results but will not result in finding your chapter.*	
AU3	Please confirm whether the presented head levels are okay in this chapter.	
AU4	For the authors ➔ GPS is redundant when using GNSS	
AU5	RUTH ➔ Harmonize the way to reference equations I THINK SPRINGER WILL DO THAT – Although I see that it is not even consistent within the chapter here - RK	